Supporting Information

Constructing Metal Telluride-Grafted MXene as Electron "Donor-Acceptor" Heterostructure for Accelerating Redox Kinetics of High-Efficient Li-S Batteries

Tianli Li, Yizhou Liu, Jian Wang, Hua Hao, Zhiyong Yu,* and Hanxing Liu*

T. Li, H. Hao, Z. Yu, H. Liu

State Key Laboratory of Advanced Technology for Materials Synthesis and Processing, School of Material Science and Engineering, International School of Material Science and Engineering, Wuhan University of Technology, Wuhan 430070, China

* Corresponding author

E-mail: yuzhiyong@whut.edu.cn (Z. Yu); lhxhp@whut.edu.cn (H. Liu)

Y. Liu

School of Information and Optoelectronic Science and Engineering South China Normal University Guangzhou 510006, P. R. China

Tianli Li and Yizhou Liu contributed equally to this work.

J. Wang

Helmholtz Institute Ulm (HIU), Ulm D89081, Germany

Experimental Section

Materials:

Tellurium powder (Te, AR. grade), N-methylpyrrolidone (NMP, AR. grade), Sulfur (S, A.R. grade), Tetraglyme ($C_{10}H_{22}O_5$, ≥99%), Lithium sulfide (Li_2S, ≥99.98 %), and Bis (trifluoromethane) sulfonimide lithium salt (LiTFSI, ≥99%) were purchased from Aladdin reagent Co., Ltd. Titanium carbide (Ti_3AlC_2, 500 mesh) was purchased from 11 Technology Co., Ltd. Binder (LA133), Polyvinylidene fluoride (PVDF), 1,3-dioxolane (DOL), and 1,2-dimethoxyethane (DME) were purchased from Suzhou Dodochem Technology Co., Ltd. Hydrochloric acid (HCl, A.R. grade), Lithium fluoride (LiF, A.R. grade), Nickel (II) chloride hexahydrate ($NiCl_2·6H_2O$, A.R. grade) was purchased from Shanghai Technology Co., Ltd. All chemicals were used without further purification.

Synthesis of MXene:

The $Ti_3C_2T_X$ suspension was synthesized in a typical approach. In generally, 2 g Ti_3AlC_2 powder was slowly added to a mixture of a certain amount of HCl and LiF under magnetic stirring in a Teflon reactor, the reaction was maintained at 40 °C for 24 h. The slurries were acquired by centrifugation at 5000 rpm until pH is neutral. Then, the precipitates were dispersed in deionized water and sonicated for 1 h under argon protection, and centrifuged to obtain $Ti_3C_2T_X$ suspension.

Preparation of NiTe$_2$@MXene:

In a typical synthesis, A certain amount of MXene suspension was dropped into $NiCl_2$ (1mol L^{-1}) solution to attain the hydrogel in a few seconds, the hydrogel was freeze-dried for 48 h to obtain 3D architecture $Ti_3C_2T_x$ aerogel (labeled as Ni^{2+}@MXene). Next, the 3D NiTe$_2$@MXene were prepared by a simple telluride process. Simply put, the 3D MXene aerogel and Te powder were placed in a porcelain boat, the tube was heated to 550 °C for 2 h to obtain product.

Preparation of the S electrode:

The CNT/S powder was mixed with sulfur (3:7 by mass) thoroughly by grinding. Then, the resulting powder was sealed in a bottle and heated at 155 °C for 12 h. Typically, the CNT/S cathodes were prepared via mixing CNT/S composite (75 wt%), carbon black

(15 wt%) as a conductive additive, and N-lauryl acrylate (LA133, 10 wt.%) as a binder dissolved in n-propyl alcohol to form a uniform slurry, which was coated on aluminum foil and vacuum dried at 50 °C for 12 h, the areal sulfur loading is about 1.3 mg cm^{-2}. The preparation of high loading sulfur cathode electrode was using the similar way as prepare sulfur cathode.

Preparation modified separator of MXene, NiTe$_2$@MXene:

The as-prepared samples (NiTe$_2$@MXene), carbon black, and 1-methyl-2-pyrrolidinone (PVDF) were evenly mixed in a ratio of 8:1:1 to form a slurry. The slurry was then coated on the surface of the commercial 2500 polypropylene (PP) separator and dried at 50 °C for 12 h. The MXene modified separator was prepared in the same way, the content of NiTe$_2$@MXene and MXene modified layer is about 0.33 mg cm^{-2}.

Physical characterization:

The morphologies and structures of the substances were characterized by scanning electron microscopy (SEM, JSM-IT300) and transmission electron microscopy (TEM, Talos-F200S). The Brunauer Emmett Taylor (BET, ASAP 2460) was used to analyze the specific surface area. The crystalline phases of all samples were examined by powder X-ray diffraction (XRD) on a Bruker D8 Advance X-ray diffractometer with Cu K$_{\alpha1}$ irradiation at 40 kV. The Raman spectrum of the products is measured using a Raman spectrometer (Raman, InVia). X-ray photoelectron spectroscopy was carried on K-Alpha$^+$, ESCALAB-250Xi XPS spectrometer. A Perkin Elmer Lambda spectrophotometer was used to determine UV–vis absorption spectra. The contact angle of various separators was tested by using a contact angle instrument (JC2000C optical).

Electrochemical tests:

The electrochemical measurements were explored using the CR2025 coin cells with CNT/S cathode, Li anode, and Celgard 2500 pp separator. The assembly of the battery is carried out in an argon-filled glovebox. The 1 M lithium bis (trifluoromethanesulfonyl) imide (LiTFSI) and 2 wt% LiNO$_3$ in DOL/DME (1:1 v/v) solvents was used as the electrolyte. The electrolyte/sulfur (E/S) ratio was maintained at ~25 μL mg -1 per cell. CV tests were carried out within a scanning range of 0.1–0.5 mV s^{-1} between 1.7 V and 2.8 V on a CHI760E electrochemical workstation (Chenhua

Instrument, Shanghai). Electrochemical impedance spectroscopy (EIS) was recorded in the range of 100 kHz–0.01 Hz with an amplitude of 5 mV using CHI 760E workstation. The galvanostatic charge-discharge curves were conducted on a Land battery-test station (Wuhan LAND Electronic Co, Ltd.) within 1.7–2.8 V voltage intervals. The Li-S pouch cell was assembled by sandwiching the NiTe$_2$@MXene separator between the sulfur cathode and Li anode followed by sealing in an Al plastic film. The pouch-cell was fabricated in an Ar-filled glove box. The size of the cathode and anode electrodes is 20 mm × 30 mm. The sulfur loading is about 2 mg cm^{-2} and the E/S ratios are kept at 17 μL mg^{-1}. The pouch cells were galvanostatically cycled at a current density of 0.1 C in the potential range of 1.7–2.8 V.

Assembly and testing of Li$_2$S$_6$ symmetric batteries:

Symmetric cells were assembled with two identical electrodes of samples loaded onto carbon paper (CP) disks. 0.2 M Li$_2$S$_6$ solution (in DME/DOL) solution was used as the electrolyte. MXene and NiTe$_2$@MXene are used for the working electrode and the counter electrode, respectively. Cyclic voltammetry (CV) tests were carried out at a scan rate of 4 mV s^{-1} between -1 V and 1 V on a CHI760E electrochemical workstation.

LiPSs adsorption test:

Sulfur and Li$_2$S are mixed in a molar ratio of 5:1, and the mixture was poured into an appropriate amount of DME/DOL (volume ratio 1:1) solution and magnetically stirred for 24 h until a dark brown Li$_2$S$_6$ solution was obtained. The equal weight of MXene and NiTe$_2$@MXene were immersed to the 3 mL of Li$_2$S$_6$ solution. The adsorption ability of samples for Li$_2$S$_6$ was further validated by Ultraviolet-visible (UV-vis) spectroscopy.

Li$_2$S nucleation test:

S and Li$_2$S were mixed in DOL/DME solvent with a volume ratio of 1:1 at a ratio of 7:1, and stirred at 60 ^{o}C for 24 h to get Li$_2$S$_8$ solution. MXene and NiTe$_2$@MXene powder was used as the working electrodes, Lithium foil serves as the counter electrode. 20 μL Li$_2$S$_8$ solution was used as an electrolyte and dropped on the cathode surface, while a blank electrolyte without Li$_2$S$_8$ was dropped on the Li metal side. The assembled battery was discharged to 2.06 V at a current density of 0.112 mA, and then

carried out constant voltage deposition experiments at 2.05 V until the current dropped below 10^{-5} A.

Li$_2$S$_6$ solution permeation test:

The permeation test of Li$_2$S$_6$ solution was performed using an H-shaped glass cell. The two tubes were separated by NiTe$_2$@MXene modified separator with an intermediate layer. A certain volume of Li$_2$S$_6$ solution was added to the right side of the glass cell, and an equal volume of DOL and DME solvent was added to the left side of the glass cell.

Calculations for diffusion coefficient of Li ions:

The coefficient of Li$^+$ diffusion is obtained through the Randles-Sevcik equation:

$$I_p = (2.69 \times 10^5) n^{1.5} A D_{Li^+}^{0.5} v^{0.5} C_{Li}$$

where I$_p$ is the peak current, n is the number of electron transfers (n = 2), A is the area of the electrode, D$_{Li+}$ is the Li$^+$ diffusion coefficient, C$_{Li}$ is the Li$^+$ concentration, and v is the CV scan rates (0.1–0.5 mV s^{-1}). There is a linear relationship between I$_p$ and v$^{1/2}$.

Computational Methods:

All density functional theory (DFT) calculations were performed using the Vienna ab initio simulation package (VASP) with exchange-correlation functional of generalized gradient approximation (GGA) of Perdew, Burke, and Ernzerhof (PBE) approach. The Projection Augmented Wave (PAW) potential was chosen to describe the ion nucleus and considered the valence electrons using a plane wave basis set with a kinetic energy cutoff of 400 eV. The convergence criteria for residual force and energy were set at 0.02 eV Å^{-1} and 10^{-5} eV, respectively. To avoid the interaction between the two periodic elements, a vacuum space of 15 A was chosen. Charge density difference was acquired from the charge difference between the substrate and the adsorbent. To unveil the adsorption ability of LiPSs on the surface of NiTe$_2$@MXene and MXene, the adsorption energies (E$_{ads}$) were calculated using the following equation:

$$E_{ads} = E_{ad/sub} - E_{ad} - E_{sub}$$

where E$_{ad/sub}$ is the total energy of Li$_2$S$_x$ (x =1, 2, 4, 6, or 8) on the catalysts interaction system, E$_{ad}$ and E$_{sub}$ are the adsorbate in the structure and the clean substrate,

respectively.

The free energy was calculated using the equation:

$$\Delta G = \Delta E + \Delta ZPE - T\Delta S$$

where ΔG, ΔE, ΔZPE and ΔS are the free energy, total energy from DFT calculations, zero-point energy, and entropic contributions, respectively.

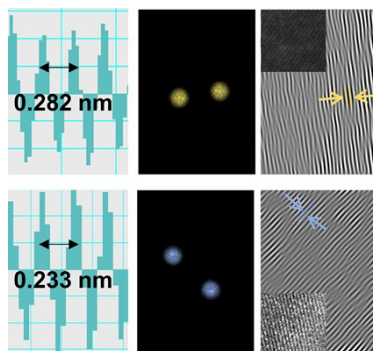**Figure S1.** Digital pictures of the Ni^{2+}@MXene hydrogel.

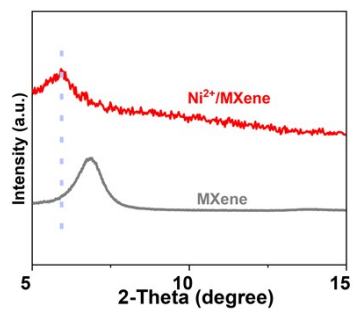**Figure S2.** FFT patterns and inverse FFT lattice patterns of MXene and $NiTe_2$.

Figure S3. XRD patterns of Ni^{2+}@MXene and MXene.
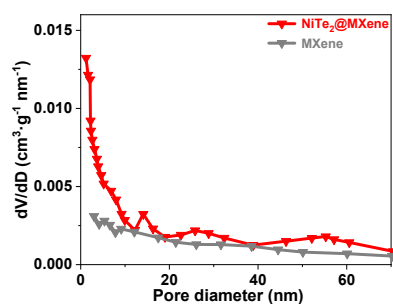
Figure S4. The pore size distribution profiles of MXene and NiTe$_2$@MXene.
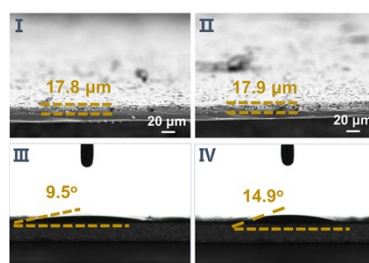
Figure S5. Cross-sectional SEM images (I-II) and contact angles between electrolyte (III-IV) for NiTe$_2$@MXene and MXene modified separators.
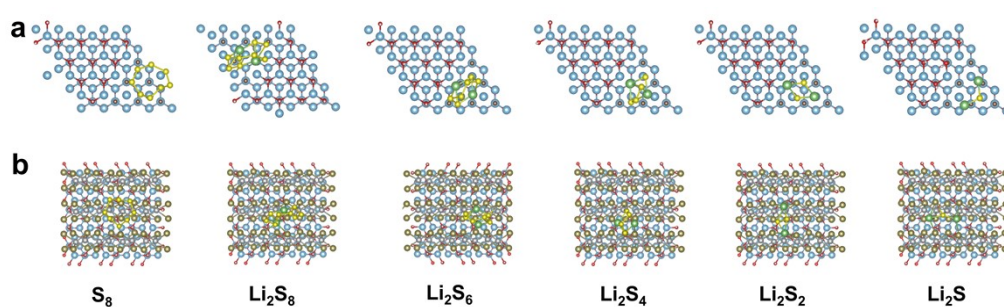

Figure S6. The corresponding optimal adsorption structure diagrams of different sulfur species (S$_8$, Li$_2$S$_8$, Li$_2$S$_6$, Li$_2$S$_4$, Li$_2$S$_2$, and Li$_2$S) on MXene a) and NiTe$_2$@MXene heterostructure b).
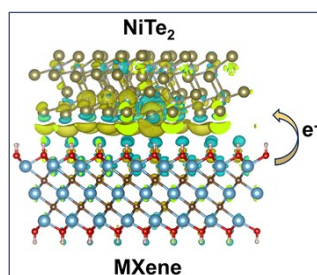
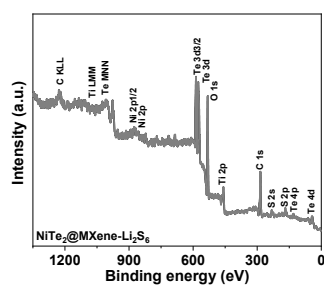**Figure S7.** Differential charge density distribution of the interaction between NiTe$_2$ and MXene.

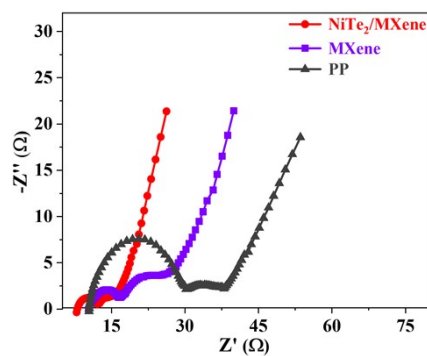**Figure S8.** The survey XPS spectrum of NiTe$_2$@MXene-Li$_2$S$_6$.
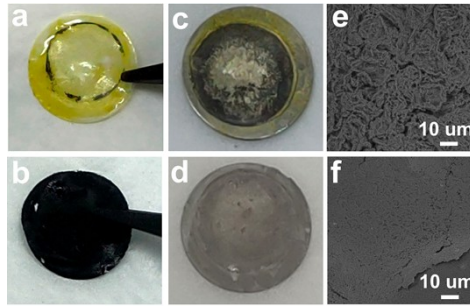

Figure S9. EIS profiles after cycling.

Figure S10. Digital pictures of a, b) separators surface and c, d) Li-metal surface. e, f) SEM images of Li-metal surface, for PP and NiTe$_2$@MXene modified separators.
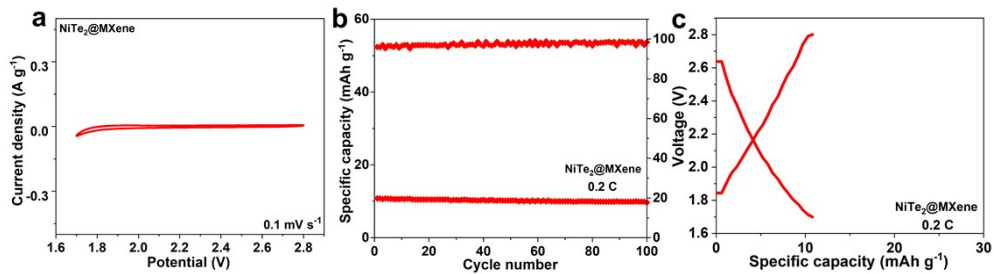

Figure S11. a) CV curve at 0.1 mV s^{-1}, b) Cycle stability tests at 0.2 C, c) galvanostatic charge/discharge curve in the voltage range of 1.7-2.8 V of the pristine NiTe$_2$@MXene cathode (without S loading).
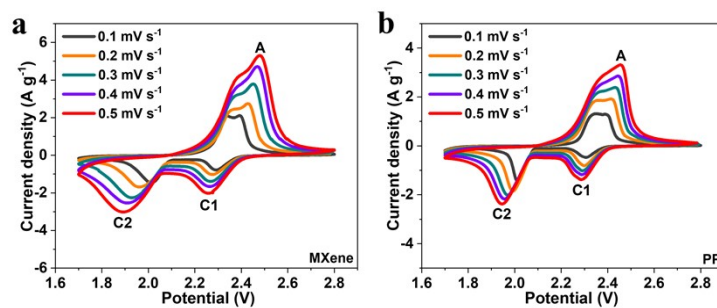

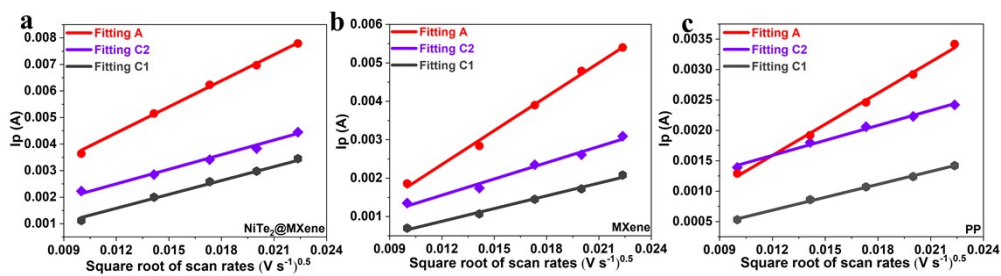**Figure S12.** CV profiles at different scan rates (from 0.1 to 0.5 mV s^{-1}) of MXene and PP.

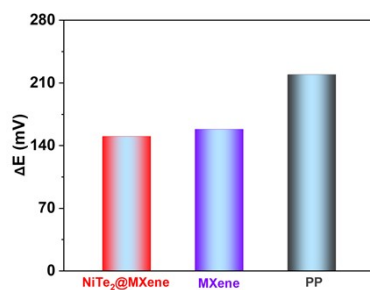**Figure S13.** Linear fits of the peak currents of NiTe$_2$@MXene a), MXene b), and PP c).

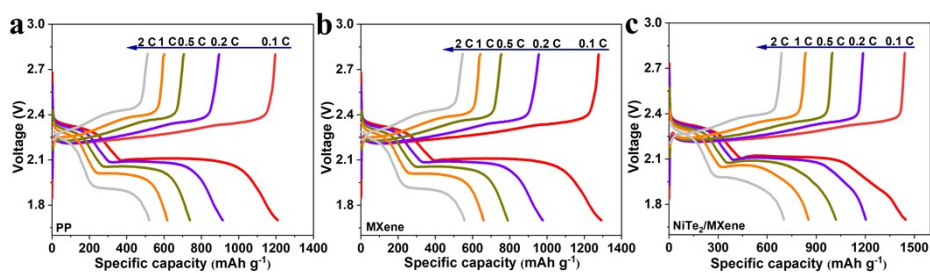**Figure S14.** ΔE calculated from the voltage curves.

Figure S15. a-c) Charge/discharge curves of the Li–S cells based on PP a), MXene b), and NiTe$_2$@MXene c).
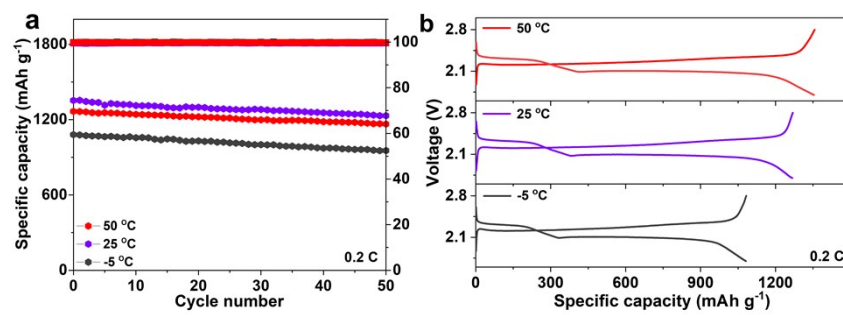
Figure S16. a) Cycling performance, and b) the corresponding discharge/charge curves at 50 °C, 25 °C, and -5 °C.

Table S1. The novelty and advantages of NiTe$_2$@MXene in Li-S batteries

Cathode	Sulfur hosts	NiTe$_2$@MXene heterostructure
	☼ Conductivity	※ Ultrahigh conductivity; ※ Alleviate volume expansion; ※ Enhance chemical storage activity and conversion reactions.
Anode	Anode protection	NiTe$_2$@MXene heterostructure
	☼ Electrolyte additives only temporarily mitigate the shuttle effect	※ Provide a permanent and physically robust framework for LiPSs adsorption and conversion.
Structural stability	Tellurides	NiTe$_2$@MXene heterostructure
	☼ Larger lattice parameters and ultrahigh conductivity； ☼ Intrinsic semiconductor properties; ☼ Easy to potential structural changes or pulverization; ☼ Tend to agglomerate.	※ Mitigate catalyst aggregation; ※ Exhibit a large specific surface area; ※ Furnishe sufficient active sites to anchor LiPSs; ※ Facilitate rapid electrolyte penetration and charge carrier transfer.

Table S2. Summary of slope at peak A, B, and C for various separators

Modified separator	NiTe$_2$@MXene	MXene	PP
Sloop at peak A (cm^2 s^{-1})	0.3272	0.2940	0.1709
Sloop at peak C2 (cm^2 s^{-1})	0.1833	0.1409	0.0821
Sloop at peak C1 (cm^2 s^{-1})	0.1741	0.1105	0.0709

Table S3. Summary of Li$^+$ diffusion coefficient for different separators

Modified separator	NiTe$_2$@MXene	MXene	PP
D$_{Li+}$ at peak A (cm^2 s^{-1})	1.849×10^{-7}	1.493×10^{-7}	5.047×10^{-8}
D$_{Li+}$ at peak C2 (cm^2 s-1)	5.800×10^{-8}	3.429×10^{-8}	1.165×10^{-8}
D$_{Li+}$ at peak C1 (cm^2 s-1)	5.233×10^{-8}	2.109×10^{-8}	8.674×10^{-9}

Table S4. Comparison of the long-term cycling performance of Li-S batteries with recently reported work.

Separator	Coating loading (mg cm^{-2})	S Loading (mg cm^{-2})	Rate capacity (mAh g^{-1})/C rate	Capacity decay rate/ cycle number/C rate	Ref.
ZnS@WCF	0.5	1	1070.4/0.5 C	0.1%/300/0.5 C	[1]
CNF/CoS/KB	0.36	1.8-2.0	900/1 C	0.076%/760/1 C	[2]
ISC/C	0.7	1.3-1.5	754.5 /1 C	0.054%/500/1 C	[3]
CAF	N/a	1.0-1.2	1096/0.2 C	0.3%/100/0.2 C	[4]
V_2O_5	0.2	1.2	1132/0.2 C	0.11%/100/0.2 C	[5]
SCOF-2	0.15	1.3-1.5	795/1 C	0.4%/800/1 C	[6]
PAA	1	1.2	442/0.5 C	0.07%/600/0.5 C	[7]
CNT/MoP$_2$	0.58	1.2	1223/0.2 C	0.152%/100/0.2 C	[8]
MnO$_2$/CNT	0.35	0.8	794.2/1 C	0.136%/500/1 C	[9]
VN	1.52	1.6	895/1 C	0.077%/800/1 C	[10]
Nb$_2$O$_5$-CNT	0.38	1.4	552/0.2 C	0.23%/100/0.2 C	[11]
NiTe$_2$@MXene	**0.30-0.32**	**1.3**	**933.5/1 C**	**0.0287%/500/1 C**	**This work**

References

1   J.-L. Yang, S.-X. Zhao, Y.-M. Lu, X.-T. Zeng, W. Lv and G.-Z. Cao, *J. Mater. Chem. A.*, 2020, **8**, 231-241.

2   Y. Yang, S. Wang, L. Zhang, Y. Deng, H. Xu, X. Qin and G. Chen, *Chem. Eng. J.*, 2019, **369**, 77-86.

3   W. Wang, Y. Yang, H. Luo, S. Li and J. Zhang, *J. Colloid Interf. Sci.*, 2020, **576**, 404-411.

4   X. Chen, Y. Huang, J. Li, X. Wang, Y. Zhang, Y. Guo, J. Ding and L. Wang, *J. Colloid Interf. Sci.*, 2020, **559**, 13-20.

5   K. Chen, G. Zhang, L. Xiao, P. Li, W. Li, Q. Xu and J. Xu, *Small Methods*, 2021, **5**, 2001056.

6   J. Xu, S. An, X. Song, Y. Cao, N. Wang, X. Qiu, Y. Zhang, J. Chen, X. Duan, J. Huang, W. Li and Y. Wang, *Adv. Mater.*, 2021, **33**, 2105178.

7   S. Song, L. Shi, S. Lu, Y. Pang, Y. Wang, M. Zhu, D. Ding and S. Ding, *Journal of Membrane Science*, 2018, **563**, 277-283.

8   Y. Luo, N. Luo, W. Kong, H. Wu, K. Wang, S. Fan, W. Duan and J. Wang, *Small*, 2018, **14**, 1702853.

9   Y. Wang, W. Liu, R. Liu, P. Pan, L. Suo, J. Chen, X. Feng, X. Wang, Y. Ma and W. Huang, *New Journal of Chemistry*, 2019, **43**, 14708-14713.

10   Y. Song, S. Zhao, Y. Chen, J. Cai, J. Li, Q. Yang, J. Sun and Z. Liu, *ACS Appl. Mater. Interfaces*, 2019, **11**, 5687-5694.

11   Y. Liu, M. Chen, Z. Su, Y. Gao, Y. Zhang and D. Long, *Carbon*, 2021, **172**, 260-271.